Online estimation of the wavefront outer scale profile from adaptive optics telemetry

A. Guesalaga,[1]⋆ B. Neichel,[2] C. M. Correia,[2] T. Butterley,[3] J. Osborn,[3] E. Masciadri,[4] T. Fusco[2,5] and J.-F. Sauvage[2,5]

[1]*Department of Electrical Engineering, Pontificia Universidad Católica de Chile, 4860 Vicuña Mackenna, 7820436 Santiago, Chile*
[2]*Laboratoire d'Astrophysique de Marseille (LAM), Aix Marseille Université, CNRS, UMR 7326, F-13388 Marseille, France*
[3]*Centre for Advanced Instrumentation (CfAI), Durham University, South Road, Durham DH1 3LE, UK*
[4]*INAF – Arcetri Astrophysical Observatory, Largo E. Fermi 5, I-50125 Firenze, Italy*
[5]*ONERA – 29 avenue de la Division Leclerc, F-92322 Chatillon Cedex, France*

ABSTRACT

We describe an online method to estimate the wavefront outer scale profile, $\mathcal{L}_0(h)$, for very large and future extremely large telescopes. The stratified information on this parameter impacts the estimation of the main turbulence parameters [turbulence strength, $C_n^2(h)$; Fried's parameter, r_0; isoplanatic angle, θ_0; and coherence time, τ_0) and determines the performance of wide-field adaptive optics (AO) systems. This technique estimates $\mathcal{L}_0(h)$ using data from the AO loop available at the facility instruments by constructing the cross-correlation functions of the slopes between two or more wavefront sensors, which are later fitted to a linear combination of the simulated theoretical layers having different altitudes and outer scale values. We analyse some limitations found in the estimation process: (i) its insensitivity to large values of $\mathcal{L}_0(h)$ as the telescope becomes blind to outer scales larger than its diameter; (ii) the maximum number of observable layers given the limited number of independent inputs that the cross-correlation functions provide and (iii) the minimum length of data required for a satisfactory convergence of the turbulence parameters without breaking the assumption of statistical stationarity of the turbulence. The method is applied to the Gemini South multiconjugate AO system that comprises five wavefront sensors and two deformable mirrors. Statistics of $\mathcal{L}_0(h)$ at Cerro Pachón from data acquired during 3 yr of campaigns show interesting resemblance to other independent results in the literature. A final analysis suggests that the impact of error sources will be substantially reduced in instruments of the next generation of giant telescopes.

Key words: atmospheric effects – instrumentation: adaptive optics.

1 INTRODUCTION

Astronomical observations using existing 10 m class telescopes and future 25–40 m extremely large telescopes (ELTs) require knowledge of the 3D atmospheric wavefront distortions in order to specify and optimize the performance of wide-field adaptive optics systems (WFAOs). WFAOs reduce the negative impact of the limited sky coverage on adaptive optics (AO) systems by means of techniques such as optical turbulence tomography.

The optimization of such systems depends on the atmospheric conditions, including the wavefront outer scale ($\mathcal{L}_0$). $\mathcal{L}_0$ gives an estimation of the spatial coherence of the wavefront and becomes significant for larger telescopes when the telescope diameter approaches this outer scale (Ragazzoni, Marchetti & Valente 2000).

Determining the spatial coherence of the atmospheric turbulence is essential for the estimation of other atmospheric parameters on large telescopes such as seeing, isoplanatic angle and coherence time (Maire et al. 2007). This has a great importance in astronomy for applications such as astrometry, interferometry, point spread function reconstruction (PSF-R), tomography and turbulence profiling (Ellerbroek 2013; Yelda et al. 2013).

Historically, it has been a common practice to represent the outer scale as a global turbulence parameter. However, some studies have shown that it can vary significantly with altitude (Maire et al. 2007; Dali et al. 2010; Ziad et al. 2013). This height-dependent outer scale, $\mathcal{L}_0(h)$, has been introduced in the phase power spectrum of a von Kármán model by Borgnino, Martin & Ziad (1992):

$$W_\phi(f, h) = 0.38\lambda^{-2}C_n^2(h)\delta h \left[f^2 + \frac{1}{\mathcal{L}_0(h)^2} \right]^{-11/6}, \quad (1)$$

⋆ E-mail: aguesala@ing.puc.cl

where f is the modulus of the spatial frequency and $C_n^2(h)$ is the turbulence strength profile. Although significant efforts have been made to estimate this parameter for site testing (Ziad 2016), no online method exists to the best of our knowledge. While estimating turbulence parameters using spatial coherence effects, the integrated outer scale $\mathcal{L}_0$ is still the de facto variable used for this purpose. For example, in the case of seeing estimation assuming a von Kármán model of turbulence, ε_{vK}, an accepted approximation is (Conan 2000; Tokovinin 2002)

$$\varepsilon_{vK} \approx \varepsilon_0 \sqrt{1 - 2.183\,(r_0/\mathcal{L}_0)^{0.356}}, \tag{2}$$

where ε_0 is the full width half maximum of the PSF for a Kolmogorov model, i.e. $\varepsilon_0 = 0.976\frac{\lambda}{r_0}$.

For the isoplanatic angle, θ_0, the effect of $\mathcal{L}_0$ is described by (Conan 2000)

$$-\frac{\pi^{5/3}\Gamma(-5/6)}{2^{1/6}}\theta_0^{5/3}\mu_{5/3} + \frac{\pi^2\Gamma(-1/6)}{2^{1/6}}\theta_0^2\mu_2\mathcal{L}_0^{-1/3}$$
$$-\frac{\sqrt{2}\pi^{5/3}\Gamma(1/3)}{\Gamma(7/6)k^2} = 0, \tag{3}$$

where $\mu_\alpha = \int_h^\infty C_n^2(h)\,h^\alpha\mathrm{d}h$ and Γ is the gamma function.

It has been shown (Fusco 2000; Jolissaint, Veran & Marino 2004) that WFAO and PSF-R can be particularly sensitive to the global $\mathcal{L}_0$ and therefore to its stratified version $\mathcal{L}_0(h)$. Furthermore, the non-stationarity characteristics of turbulence require simultaneity in the estimation of $C_n^2(h)$ and $\mathcal{L}_0(h)$. The aim of this work is to develop an online method for the complete characterization of the turbulence profile (strength and special coherence) so that it can be effectively used in the optimization of AO loops and also as a tool for post-processing applications such as PSF-R methods.

In the following section, we present a method based on the SLO-DAR technique (Butterley, Wilson & Sarazin 2006) to estimate the 'overall' $\mathcal{L}_0$ from on-axis AO telemetry data. First, the goal is to highlight the limitations of SLOpe Detection And Ranging (SLODAR) when used for this purpose and, secondly, to motivate the need of a $\mathcal{L}_0(h)$ profiler using multiple wavefront sensors (WFSs) available in WFAO configurations.

1.1 Estimating the integrated $\mathcal{L}_0$

Here, we describe the technique to estimate the global $\mathcal{L}_0$ using telemetry data from the Gemini South 8 m telescope and its multiconjugate adaptive optics (MCAO) system, GeMS (Neichel et al. 2010). It is based on the auto-correlation of slopes acquired from the laser guide star (LGS) WFSs.

The first step in the method consists in computing a set of simulated or theoretical auto-correlation functions for different values of $\mathcal{L}_0$s that are later used to fit the auto-correlation function obtained from LGS telemetry. The object-oriented MATLAB adaptive optics (OOMAO) package (Conan & Correia 2014) has been used to simulate the phase screens. OOMAO is based on a small set of classes representing the source, atmosphere, telescope, wavefront sensor, deformable mirror and an imager of an AO system.

Fig. 1 shows simulated auto-correlation cuts for an 8 m telescope and for different outer scale values, $\mathcal{L}_0 = \{1, 5, 10, 20, 30, 40, 50\}$ m. Note that for large values of $\mathcal{L}_0$, the functions become broader and they asymptotically converge to the same shape. This means that the technique is insensitive to $\mathcal{L}_0$ changes when the pupil diameter is smaller than the largest turbulence eddy. We have found that for methods based on the SLODAR technique, no significant differences in the auto-correlation functions can be obtained for
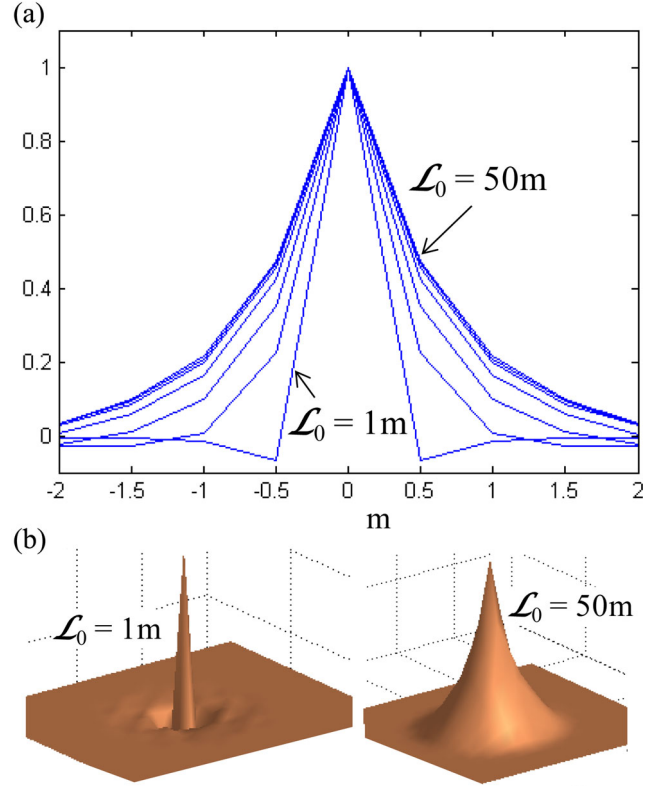

Figure 1. Simulated auto-correlations of slopes from GeMS. (a) Slices of normalized responses for $\mathcal{L}_0 = \{1, 5, 10, 20, 30, 40, 50\}$ m. (b) 3D representation of response function for outer scales of 1 and 50 m.

values of $\mathcal{L}_0$s of about three to four times the size of the pupil (see also Butterley, Osborn & Wilson 2015).

As GeMS is a closed-loop system, the next step is to construct the pseudo-open-loop slopes (POLSs) from on-sky data using the actuator voltages, the interaction matrix and the residual slopes (see Cortés et al. 2012 and Guesalaga et al. 2014 for a detailed explanation). After subtracting tip and tilt, these slopes are used to construct the auto-correlation of slopes using the normalization of overlapping subapertures described in Butterley et al. (2006) and Wang, Schöck & Chanan (2008).

The first problem to face is that the noise generated by the detectors will auto-correlate perfectly at the centre of these functions (see Fig. A1). Three alternatives to reduce this problem are described in the Appendix: (i) fitting a theoretical auto-correlation function to the one obtained from telemetry data, but leaving out the central element in the matrix; (ii) subtracting the high-frequency noise estimated from temporal power spectra of slopes and (iii) correlating slope frames with their one-cycle delayed sample. We have found that the latter outperforms the other options.

Fig. 2 shows two examples of auto-correlation functions obtained from GeMS on-sky telemetry. The first case (top) can be represented by a single theoretical auto-correlation function, so a common outer scale can be associated with it. The second case (bottom) is a more complex response where a single outer scale cannot represent it adequately. In fact, after eliminating the effect of noise in the telemetry data and using fitting techniques, two or more functions with different outer scale provide a much better representation. The sharper component could be caused by dome seeing (Guesalaga et al. 2014) or ground turbulence (Dali et al. 2010).
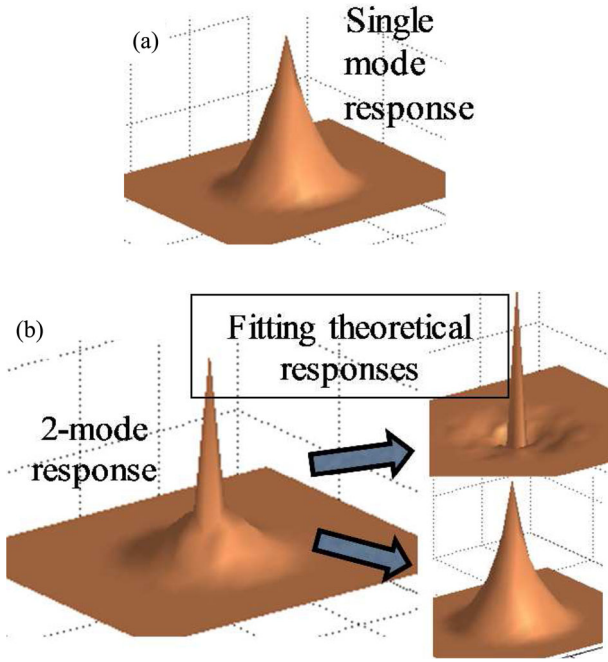
Figure 2. Examples of auto-correlations of slopes from GeMS telemetry: (a) single mode function (2014 February 13 04:56:16); (b) two-mode function (2013 April 18 06:05:50).

This means that the use of a single $\mathcal{L}_0$ is not adequate to describe the spatial coherence of the atmosphere, since the response function can be the result of combining slopes from more than one layer, each with different outer scale values, i.e. a profile or $\mathcal{L}_0(h)$ (Coulman et al. 1988; Lukin, Fortes & Nosov 1998; Dali et al. 2010; Ziad et al. 2013).

2 A PROFILING METHOD FOR $\mathcal{L}_0(h)$

Next, we develop a novel technique to estimate $\mathcal{L}_0(h)$ and test it using telemetry data collected with GeMS during 3 yr of campaigns. This extension of the method described in the previous section is also based on the SLODAR triangulation technique and is illustrated in the simplified diagram of Fig. 3, for a case of two WFSs that are cross-correlated to generate functions that depend on the overlapping turbulence patch common to both sensors. The correlation peaks shift along the baseline connecting the two WFSs by an amount proportional to the altitude of the layer (Fig. 3, right). Then, the turbulence profile can be recovered from this correlation map. In WFAO systems, such as GeMS, cross-correlations of slopes are obtained from more than two WFSs.

An immediate advantage of using cross-correlations is that each sensor contains independent noise, so their impact on the cross-correlation functions becomes negligible for large sets of slope frames. In the method described in Section 1.1, the latter is not the case as the noise correlates perfectly to the auto-correlation functions as illustrated in Fig. A1.

In the GeMS configuration, five WFSs receive light from an asterism composed of five sodium LGSs having an 'X' shape (Neichel et al. 2010). By computing the cross-correlation of POLS (after removing tip and tilt), a matrix corresponding to the combined effects of the telescope and atmospheric turbulence transfer functions is obtained. This response is a function of altitude h, the turbulence strength $C_n^2(h)$ and its stratified spatial coherence $\mathcal{L}_0(h)$. By fitting individual theoretical responses of layers with different strengths,
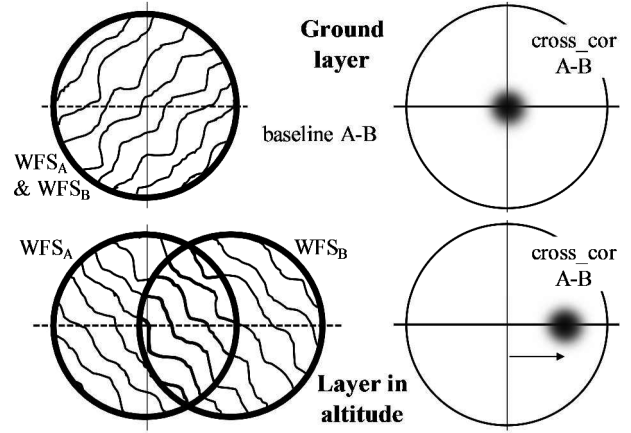

Figure 3. Simplified schematic of the SLODAR technique. The atmospheric turbulence profile is recovered from the correlation of wavefront slopes of two stars (A and B) with a known angular separation. The common turbulence patch between two WFSs for a single layer (left) decreases as a function of the layer altitude; the slant range to the sodium layer (zenith angle); and the angular separation between the artificial stars (see Cortés et al. 2012). This causes the correlation peak to shift along the WFS baseline (bottom right). For the five LGSs of GeMS, multiple cross-correlations of WFSs pairs are averaged to get better cross-correlation functions.

altitudes and outer scales, the profiles $\mathcal{L}_0(h)$ and $C_n^2(h)$ can be simultaneously estimated from the measured data.

2.1 GeMS's response functions

As explained before, the method identifies the parameters of each layer by fitting simulated functions to the response constructed from telemetry. We call the simulated 'response' functions $C_{\rm rsp}(\mathcal{L}_0,h)$ and they are normalized to have the same $C_n^2(h)$ value. Unfortunately, due to the combined effects of telescope's aperture, fratricide masking and Fresnel propagation, the $C_{\rm rsp}(\mathcal{L}_0,h)$ functions are extremely complex to be modelled analytically, so we use a Monte Carlo simulation approach to compute them and store them in a 2D array (mode basis) that contains the responses for N_H altitudes and N_L outer scales.

Adding the dimension corresponding to altitude h in the array is not obvious and the reasons for this are as follows:

(1) Cross-correlation of slopes varies with altitude (Butterley et al. 2006). Also, the fratricide effect caused by sodium scattering in LGS (e.g. GeMS) generates further asymmetries in the response function even at the ground.

(2) It has been shown (Goodwin, Jenkins & Lambert 2007; Tokovinin & Kornilov 2007) that propagation effects from higher layers are significant for subaperture diameters smaller than 0.2 m. Errors as high as 30 per cent are possible in the tip and tilt variances propagated from a layer at 10 km. In this case, the weak turbulence assumption does not hold and Fresnel propagation must be assumed. This effect also calls for a differentiation of correlation functions in altitude as the degree of diffraction will depend on the propagation distance. We have performed several simulations for the GeMS case in order to quantify the impact of the propagation on the resulting slopes, but found no significant effect. For the worst case, the ratio between the rms values of the slope differences and the rms of the raw slopes obtained from a wavefront propagated from a layer at 10 km was less than 0.04 per cent. This is not surprising, as the averaging effect of GeMS's 0.5 m diameter subapertures on the
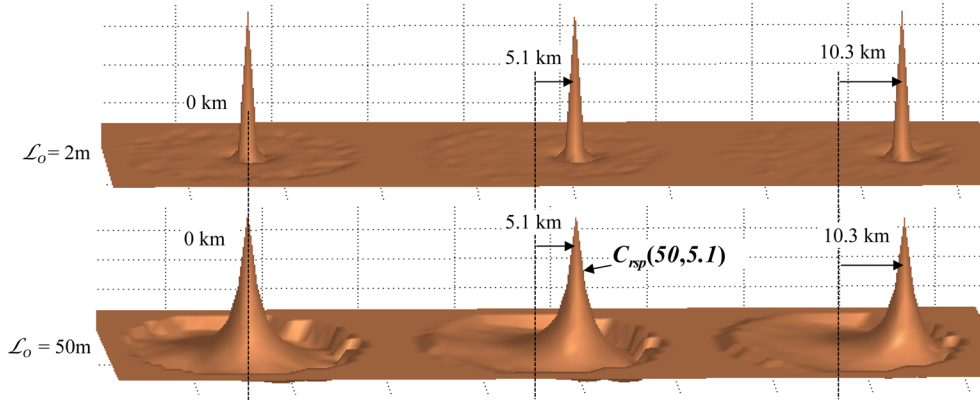
Figure 4. Simulated $C_{rsp}(\mathcal{L}_0, h)$ functions for three altitudes (columns) and two values of outer scale (rows). The asymmetries at the ground and higher altitudes are due to the finite nature of the telescope pupil and the WFS fratricide effect.
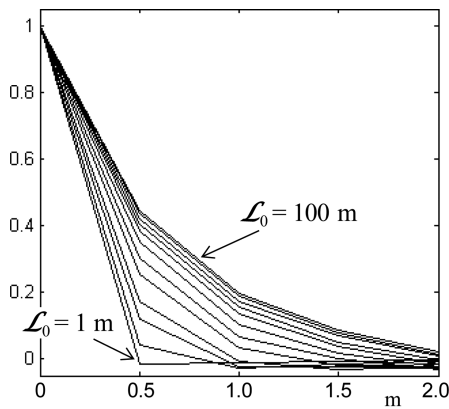

Figure 5. Cross-section of ground layer response functions for $\mathcal{L}_0$: {1, 2, 3, 4, 6, 8, 11, 16, 22, 32, 50, 100}. The differences in shape are marginal at the higher end of the range.

slopes is much stronger than the effect of the turbulence transfer function due to a seeing of, say, 0.2 m.

Fig. 4 shows six cases of $C_{rsp}(\mathcal{L}_0, h)$ for altitudes of 0, 5 and 10 km and for outer scales of 2 and 50 m, assuming GeMS configuration parameters. These correlation functions shift along the baseline connecting the two WFSs for higher altitudes (Fig. 3, right), but they also change in shape, especially for larger outer scales. These differences in shape are caused by the finite nature of the telescope pupil and the WFS fratricide effects (Cortés et al. 2012). These characteristics are nicely captured via simulation.

2.2 Selection of altitudes and outer scales for the response functions

For GeMS, we choose altitude layers separated by about 350 m, which is roughly a fifth of the separation between altitude slabs defined by the subaperture diameter (Cortés et al. 2012). In our case, we have limited N_H to 50 layers, which gives a range between 0 and 17.2 km.

The selection of the set for outer scale values in $C_{rsp}(\mathcal{L}_0, h)$ is more complex. As shown in Fig. 5 (for a turbulence layer at the ground), the response functions vary significantly for the smaller outer scales. For larger values of $\mathcal{L}_0$, however, these changes become marginal. This suggests that an array of $C_{rsp}(\mathcal{L}_0, h)$ following a logarithmic distribution of $\mathcal{L}_0$ sizes would give a more representative set, so for

the case of GeMS we have chosen $\mathcal{L}_0$: {1, 2, 3, 4, 6, 8, 11, 16, 22, 32, 50, 100}. Note that even using this logarithmic distribution, the curves get asymptotically similar as they approach the higher end of the outer scale range. This is due to the finite aperture of the telescope that becomes insensitive to $\mathcal{L}_0$ values, much larger than its diameter.

The method consists of two steps: first, a search for the best fit among the finite discrete values of $\mathcal{L}_0$ and h is carried out. Secondly, a stage in the optimization relaxes this discrete restriction by looking for a function $C_{rsp}(\mathcal{L}_0, h)$ that is a linear combination of neighbour functions, i.e. a 2D interpolation within the array:

$$
\begin{aligned}
C_{rsp}(\mathcal{L}_0, h) = \\
\left((1-\alpha)C_{rsp}(\mathcal{L}_0^i, h^j) + \alpha C_{rsp}(\mathcal{L}_0^{i+1}, h^j) \right)(1-\beta) \\
+ \left((1-\alpha)C_{rsp}(\mathcal{L}_0^i, h^{j+1}) + \alpha C_{rsp}(\mathcal{L}_0^{i+1}, h^{j+1}) \right)\beta,
\end{aligned} \tag{4}
$$

where $i = \{1, \ldots, N_L\}$ and $j = \{1, \ldots, N_H\}$. Weightings α and β are in the range [0,1] and construct the interpolated $C_{rsp}(\mathcal{L}_0, h)$ to be used in the fitting process.

2.3 The fitting problem

The solution to the optimal fitting can be mathematically expressed as the minimization of the error given by

$$
\operatorname*{Min}_{\omega, \mathcal{L}_0, h} \left\langle \left(C_{meas} - \sum_{i=1}^{N_Z} \omega_i C_{ref}^i(\mathcal{L}_0, h) \right)^2 \right\rangle, \tag{5}
$$

where C_{meas} is the cross-correlation function computed from telemetry data and ω_i ($i = \{1, \ldots, N_Z\}$) are the weightings for each of the N_Z layers considered in the fitting. The choice of N_Z is given by the number of atmospheric layers that can be effectively estimated, given the number of independent elements in C_{meas}. This limitation is later analysed in Section 3.

Fig. 6 shows the window where the fitting is carried out (rectangular box). Either pixels outside this area correspond to negative altitudes or their signal-to-noise ratio is too low due to the reduced overlapping between WFSs at very high altitudes.

Once C_{meas} is constructed, the search for the optimal $\mathcal{L}_0, h$ and ω is carried out using a search algorithm known as trust-region-reflective (Moré & Sorensen 1983; Coleman & Li 1996). Fig. 7 illustrates this process, where the values of α and β (equations 4 and 5) are slaved
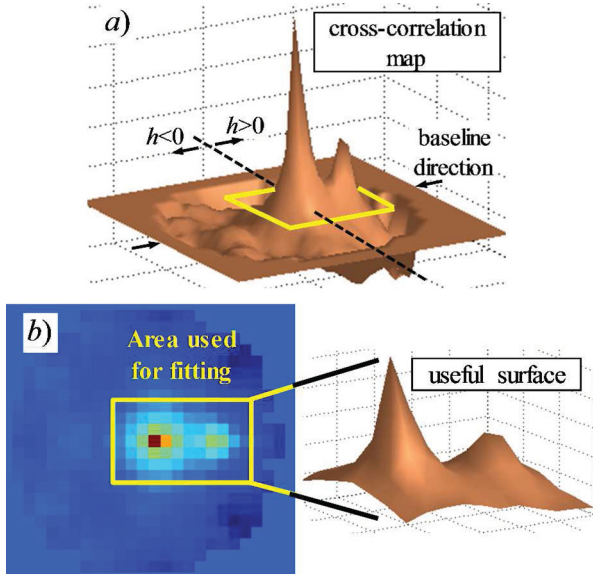
Figure 6. Area used for fitting (rectangular box). (a) Full cross-correlation map; (b) area used for fitting. On-sky data from 2013 May 22 02:41:12.
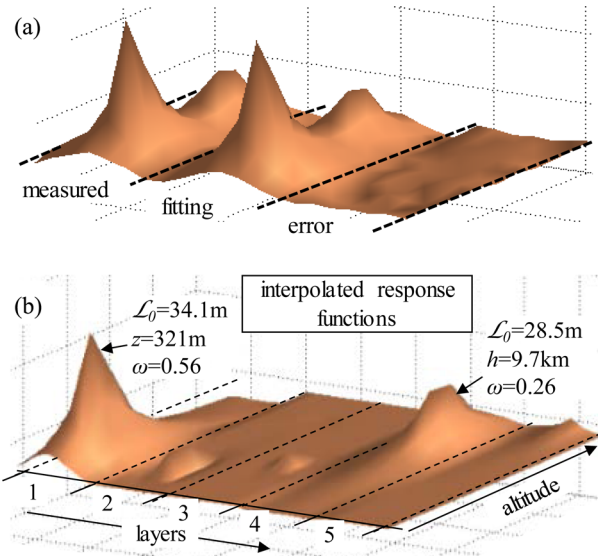

Figure 7. Fitting $C_{rsp}(\mathcal{L}_0,h)$ functions to C_{meas} (from on-sky data, 2013 May 22 02:41:12): (a) C_{meas}, fit and fitting error; (b) Interpolated $C_{rsp}(\mathcal{L}_0,h)$ functions for the five layers.

to $\mathcal{L}_0$ and h, respectively. The optimization technique is particularly suited for this problem as it can handle the minimization of quadratic functions subject to bounds on some of the unknowns. In the case of ω, a non-negativity restriction must be met. For h and $\mathcal{L}_0$, lower and upper bounds exist. The altitude spans from 0 km to the maximum detectable range defined at 17.2 km and it is given by the minimum required overlapping of the WFSs at high altitudes. For the outer scale, the minimum and maximum are, respectively, 1 and 100 m.

The search looks for a combination of $C_{rsp}(\mathcal{L}_0, h)$ that fits C_{meas}. The three surfaces in Fig. 7a (separated by dashed lines) correspond to (i) C_{meas}, the measured cross-correlation obtained from the WFS telemetry; (ii) the weighted sum of the five $C_{rsp}(\mathcal{L}_0, h)$ found in the fitting (centre); and (iii) the difference between the left and centre surfaces (right). Fig. 7b shows the result of the search for

Table 1. Turbulence parameters for the case of study. On-sky data from 2013 May 22 02:41:12.

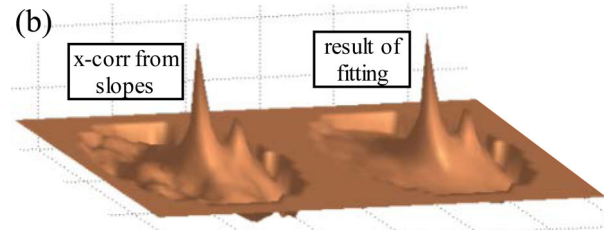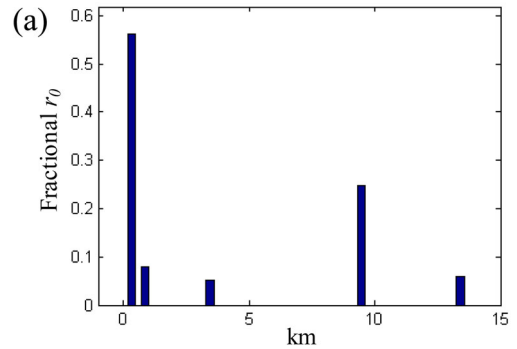| Layer | Fitting parameters | | |
	h (m)	ω	$\mathcal{L}_0$ (m)
5	13 420	0.06	22.7
4	9743	0.26	28.5
3	3295	0.04	5.1
2	672	0.08	8.8
1	321	0.56	34.5

Figure 8. Result for the case of study: (a) turbulence profile for the case of study (fractional r_0); (b) full view of the measured and fitted cross-correlation functions.

$N_Z = 5$, where the fitted functions are separated in their basis constituents.

Table 1 lists the parameters found for the five layers which when combined and subtracted to C_{meas} give the minimum error defined in equation (5). The table provides the turbulence profile (fractional r_0) via the weights (ω_i^*) of the response functions found. Having also the values of $\mathcal{L}_0$ and altitudes for each layer, the atmosphere is fully characterized.

Fig. 8a shows the associated profile obtained for this example. Note that the layers identified are described as single bars located in a continuous altitude scale, different from the standard discrete slabs found either in online profilers (Cortés et al. 2012) or those used in external monitors (Tokovinin & Kornilov 2007). Fig. 8b is a full view of the measured and fitted cross-correlation functions.

2.4 Case with two extreme $\mathcal{L}_0$ values at the ground

An interesting case is when two layers with different outer scale values co-exist at very similar heights. This is the case for the profile estimated in Fig. 9. A strong layer with 50 m outer scale is merged with another having an outer scale of approximately 1 m. Note that this situation can also be seen in the auto-correlation function, where a shoulder in the skirt of the auto-correlation function appears (Fig. 9a). The method works extremely well under these circumstances, with a clear distinction of the neighbour layer (Fig. 9b).
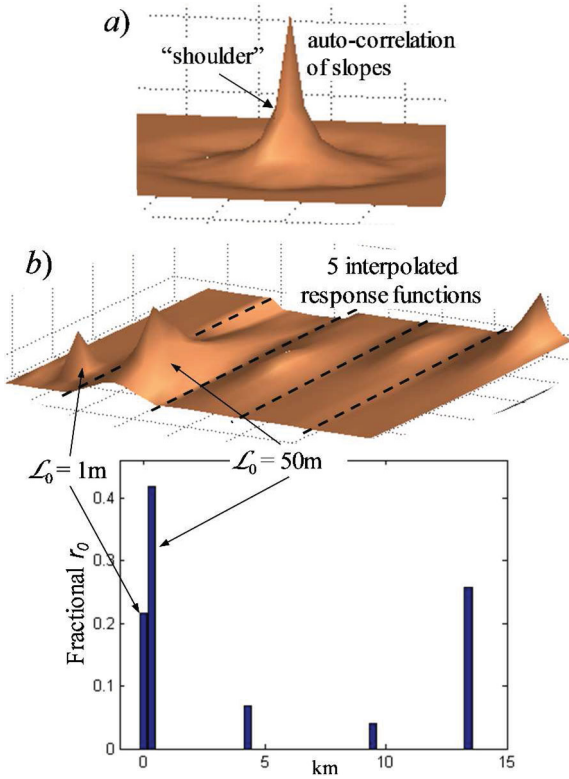
Figure 9. Case of two adjacent layers close to the ground with different outer scale values: (a) auto-correlation function where a shoulder suggests the existence of more than one value of $\mathcal{L}_0$; (b) response functions and profile resulting from the fitting. On-sky data from 2013 April 18 06:05:50.

2.5 Calculating the integrated $\mathcal{L}_0$

Once the turbulence strength profile $C_n^2(h)$ and the height-dependent outer scale $\mathcal{L}_0(h)$ have been computed from the method described above, a more reliable global outer scale $\mathcal{L}_0$ can be estimated from (Borgnino 1990)

$$\mathcal{L}_0 = \left[\frac{\int_0^\infty \mathcal{L}_0(h)^{-1/3} C_n^2(h) \, \mathrm{d}h}{\int_0^\infty C_n^2(h) \, \mathrm{d}h} \right]^{-3}. \tag{6}$$

This estimate can still be of significant value in current methods of tomographic AO and PSF-R.

3 QUANTIFYING THE ESTIMATION ERROR OF TURBULENCE PARAMETERS

During the development of the method, we have found two important sources of error that need a closer analysis. They are (i) the convergence problem due to temporally correlated slopes (see Butterley et al. 2015); and (ii) the observability of the turbulence parameters depending on the actual number of layers to be characterized.

3.1 Convergence error

The profile is strongly affected by the temporal correlation among the slopes to be processed. For example, the data from a sequence of slopes caused by slowly moving wind or by high sampling rates yield poor correlation maps. On the contrary, layers moving at high speed or slopes sampled at lower frame rates (more statistically independent) feed the profiler with high-quality data. One might
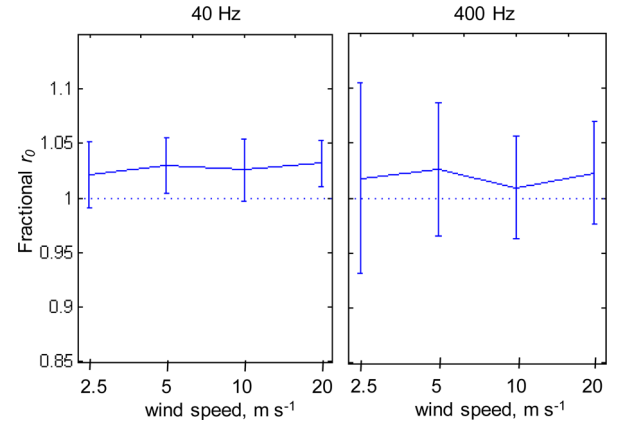

Figure 10. Estimation errors in the turbulence strength for four wind speeds and 4×10^3 frame sequences. The continuous line corresponds to the mean value of the estimations and the error bars correspond to the standard deviation in each case. An overestimation of around 2–3 per cent is observed in both cases, and significantly larger deviations result in the higher frequency case due to the stronger correlation among the samples.

think that extending the length of each sequence would solve the problem. Unfortunately, this contradicts the principle of stationarity of the turbulence analysed, i.e. the larger the sequence in time, the higher the risk that the atmospheric parameters [e.g. $C_n^2(h)$, $\mathcal{L}_0(h)$] will change during the acquisition time.

To study this convergence effect on the estimation error, we test the method via simulations, spanning different values for sampling rate, wind speed, outer scale and altitude of layers.

A total of a 100 turbulence sequences were generated using the following parameters:

(1) Outer scales: 4.5, 12.7 and 41.3 m;
(2) Layer altitudes: 0.24, 5.1, 10.1 km;
(3) Frame rate: 40 and 400 Hz;
(4) Size of slope sequence: 4×10^3 frames;
(5) Phase screens moving at wind speeds of 2.5, 5, 10 and 20 m s^{-1};
(6) Noise (photon flux): virtually no noise;
(7) r_0: 20 cm.

Fig. 10 shows the mean value and error bars when estimating the fractional r_0 of each layer for the different wind speeds. For a constant set size of 4×10^3 frames, the elapsed time is 100 s for 40 Hz sampling and 10 s for the 400 Hz sampling.

The results show that the accuracy in the mean value is within 3 per cent of the real values for both sampling rates; however, the standard deviations (error bars) are clearly unsatisfactory for the 400 Hz case. Increasing the length of the sequences would reduce the deviations in the measurements, although the stationarity assumption on the turbulence statistics might no longer hold.

It is important to emphasize that this problem is not only related to our method, but it is also a common statistical characteristic to any technique that intends to estimate turbulence parameters from temporarily correlated data (Butterley et al. 2015).

A similar analysis was done for the estimation error in the layer altitude. Fig. 11 shows that the altitude converges to the real value within a margin of ± 20 m with a significantly better performance for the 40 Hz case. In this case, the convergence error is not significant considering that the resolution given by the measuring element size (the subaperture diameter) is equivalent to 1.5 km (Cortés et al. 2012). This improvement in the resolution is obtained thanks
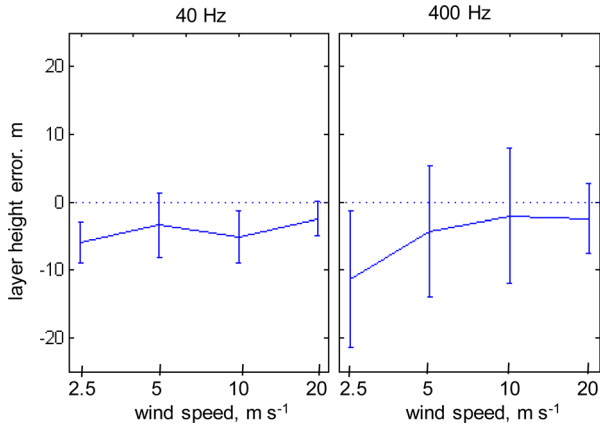
Figure 11. Estimation errors in the layer altitude for different wind speeds. The continuous line corresponds to the mean value of the estimations, whereas the error bars represent the standard deviation in each case. An underestimation of less than 6 m is observed for the slower frame rate and up to about 10 m for the faster sampling rate.
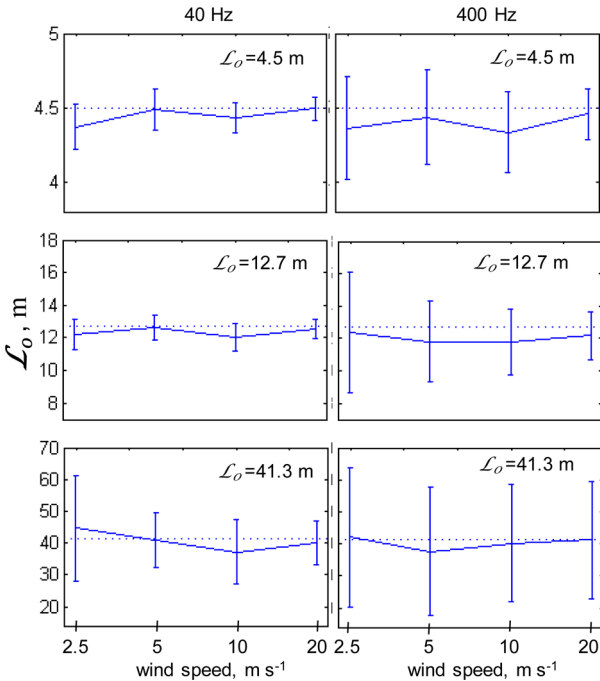

Figure 12. Estimation for three different outer scales (4.5, 12.7 and 41.3 m) from simulated data. Good performances are observed for $\mathcal{L}_0 = 4.5$ m for the two frame rates with errors in the mean and standard deviation below 0.2 and 0.7 m, respectively. For $\mathcal{L}_0$ values of 12.7 and 41.3 m, the mean error is still very good; however, the standard deviations are extremely high for the combination of high sampling rate and low wind speeds.

to the multiple subapertures used in the response function calculations and is similar to the 'sub-pixel' resolution obtained for WFS centroid calculations. The standard deviations in each case are also within adequate ranges, i.e. below 5 and 10 m for 40 and 400 Hz, respectively.

The error analysis for the estimation of $\mathcal{L}_0(h)$ was separated for three different values (4.5, 12.7 and 41.3 m). The method showed a very good convergence for the mean value, with a tendency to underestimate the simulated values (see Fig. 12).

The most important result in this analysis is that the standard deviation becomes extremely high for the two larger values of $\mathcal{L}_0$,

especially at the higher sampling rate and the lower wind speeds. Recalling Fig. 5, this is not surprising, since for cross-correlation functions, the simulated responses get very insensitive to variations in $\mathcal{L}_0$ when the values are much higher than the telescope diameter. This means that the reverse occurs when estimating $\mathcal{L}_0$ starting from the auto-correlation functions, i.e. the results will be extremely sensitive to disturbances contained in the slopes used to construct the response functions. Nevertheless, Fig. 12 shows a very accurate estimation of $\mathcal{L}_0$ for small values (less than or similar to the telescope diameter) with standard deviations in the order of centimetres. These results make sense since, even in a static condition (zero wind), the spatial frequencies are larger than the inverse of the telescope diameter, providing richer statistically independent information. The latter is not the case for large values of $\mathcal{L}_0$ where an instantaneous frame of slopes within a pupil cannot provide by itself enough information about turbulence eddies that are much larger than the telescope diameter.

3.2 Number of observable layers

The size of the dataset that the method uses to solve the inversion problem of finding the parameters for every layer in the turbulence below the LGS is given by the number of uncorrelated pixels contained inside the rectangular box defined in Fig. 6. Nevertheless, this window is symmetric with respect to the baseline between a pair of WFSs, so the number of available pixels in elements used for the fitting is only $4 \times 12 = 48$. Furthermore, not all of them have the same quality in terms of statistical independence or signal-to-noise ratio. On the other hand, the number of parameters to be estimated from these elements depends on the number of layers, i.e. if three parameters ($\mathcal{L}_0$, h and ω) characterize each layer, then the total number of unknowns to be estimated is $3 \times N_Z$. The question then is what is the maximum number of layers that can be completely described from the available data before the fitting problem becomes underdetermined? The answer is not simple, as it is obvious that the elements closer to the baseline will bear much better information than those around the perimeter of C_{meas}.

We think that the only way to determine this limit is via simulations; so we have carried out this multiple parameter estimation of a simulated profile that could tell us about the maximum number of layers (N_Z) that can be observed.

Three cases of turbulence with four, five and six layers were generated, each with 30 sets of 4×10^3 uncorrelated phase screens and their respective slopes according to the following general parameters:

(1) Source magnitude: 15;
(2) Read-out noise: 1 photoelectron per frame per pixel;
(3) Fried's parameter, $r_0 = 20$ cm.

The specific parameters ($\mathcal{L}_0$, h and ω) for each case are defined in Table 2; they have been arbitrarily chosen, similar to those reported in Ziad et al. (2013) and Maire et al. (2007). The table summarizes the results for the estimations of $\mathcal{L}_0$, h and ω, and case 1 (turbulence with four layers) is also plotted in Fig. 13.

The performance of the method is generally very good for the first two cases (four and five layers), with the exception of the outer scale, in which, for values larger than the telescope diameter, the errors exceed 10 per cent (see the error bars in Fig. 13b for the case of four layers). This is not surprising and is in agreement with the insensitivity of the response function (Fig. 5) to the higher values of outer scales. In this example, the errors in the estimation of $\mathcal{L}_0$

Table 2. Turbulence parameters ($\mathcal{L}_0$, h and ω) used for the three cases simulated and estimation errors (mean and standard deviation).

Layer	H [km]	e [m]	σ [m]	$\mathcal{L}_0$ [m]	e [m]	σ [m]	ω [1/1]	e [1/1]	σ [1/1]
4 Layers									
1	0.06	8	25	3.6	0.1	0.1	0.4	0.02	0.011
2	1.59	−10	41	40.7	0.7	11.3	0.35	0.01	0.009
3	6.23	−17	12	9.7	2.5	2.7	0.1	0.01	0.004
4	10.5	16	28	20.7	−2.9	3.5	0.15	−0.01	0.004
5 Layers									
1	0.06	12	21	3.0	0.1	0.3	0.35	0.01	0.023
2	1.59	−31	36	40.7	4.5	13.4	0.25	0.03	0.007
3	5.23	24	23	8.1	1.9	1.3	0.15	−0.01	0.014
4	8.46	−19	17	10.2	1.1	3.2	0.1	−0.03	0.040
5	11.2	43	45	13.4	−3.7	4.8	0.15	−0.02	0.032
6 Layers									
1	0.06	11	38	3.2	0.5	1.2	0.30	0.03	0.06
2	1.20	27	31	7.7	−2.8	2.7	0.15	0.02	0.03
3	4.50	−75	92	38.0	6.3	19.4	0.10	0.04	0.07
4	7.20	−53	69	25.6	7.5	15.4	0.15	−0.06	0.04
5	9.50	25	48	10.7	−1.9	3.9	0.20	0.04	0.02
6	11.6	89	126	12.9	−6.1	4.4	0.10	−0.08	0.06

at the second layer also affect the estimation of the altitude of this layer as Fig. 13 shows.

For the third case (six layers), a clear deterioration in the accuracy emerges, pointing at the observability problems imposed by the limited number of independent elements of C_{meas}.

An interesting result, obtained from estimating the fractional r_0, is that the error in the sum of contributions from all layers is always less than 3 per cent for the three cases simulated.

4 RESULTS FOR $\mathcal{L}_0(h)$ FROM GeMS TELEMETRY

A significant amount of on-sky data collected with GeMS during 3 yr of campaigns at Cerro Pachón (2012–2014) has been reduced to gather some statistics of $\mathcal{L}_0(h)$. The data files are 4×10^3 frames long, taken at different frame rates from 200 to 400 Hz.

Based on the error analysis in the previous section, we conclude that the turbulence can be accurately represented by five layers, so we apply the method to GeMS telemetry data using $N_Z = 5$.

The results obtained for 1124 samples (out of 529 circular buffers) are presented in Fig. 14, where the altitude range is divided in slabs of 2 km. Abundant data were obtained for the first division closer to the ground that allowed us to further divide this segment into two 1 km slabs.

An average of 24.0 m and a median of 17.5 m were obtained for the complete set of $\mathcal{L}_0$ samples. However, we think that these two global values have to be taken with care for two reasons: (i) the estimation range has been intentionally limited to 50 m due to the telescope blindness for large values of $\mathcal{L}_0$; and (ii) in many altitude segments, multimode histograms are found, making a single scalar parameter meaningless. Instead of using these statistical indices, we present the results using histograms of eight segments. The convenience of doing so is shown in Fig. 14(bottom) (histogram of the first 1 km slab) that clearly shows at least two modes at both extremes (1 and 50 m).

As mentioned before, the telescope size imposes a limit in the largest measurable $\mathcal{L}_0$ to no more than three or four times its diameter. In practice, this is not a problem for an online profiler, as the results are meant to feed internal processes such as AO tomography,

predictive control and PSF-R post-processing. In other words, the 'users' will not be affected by this blindness as larger values of $\mathcal{L}_0$ will be seen as tilt and treated as such.

It is also interesting to note that in the absence of online $\mathcal{L}_0(h)$ profilers, a de facto value for AO-related algorithms and PSF-R post-processing is around 20 m (Martin et al. 2000; Dali et al. 2010). This value is still measurable within reasonable accuracy with our technique that will improve for the case of future giant telescopes, which will be able to see outer scales well beyond 50 m.

The profile in Fig. 14 has many characteristics common to other previously reported profiles obtained in independent campaigns (Dali et al. 2010; Ziad et al. 2013), where the maximum values of $\mathcal{L}_0$ are obtained for altitudes between 1 and 2 km and the minimum values are located between 2 and 4 km.

It is interesting to note that for the full set of 529 circular buffers containing 1124 samples that form the profile in Fig. 14, only in 4 cases, the 5 layers accounted for less than 98 per cent of the total turbulence strength, suggesting that $N_Z = 5$ suffices to represent the turbulence accurately.

5 CONCLUSIONS

An automated technique to estimate a complete turbulence profile has been developed. It estimates not only the turbulence strength in altitude, $C_n^2(h)$, but also the outer scale for each layer, $\mathcal{L}_0(h)$. The method can be easily adapted to other WFAO systems such as Adaptive Optics Facility (Arsenault et al. 2012), CANARY (Morris et al. 2014), RAVEN (Lardière et al. 2014), ARGOS (Mazzoniet et al. 2014) or the New Solar Telescope MCAO for solar AO (Schmidt et al. 2014).

We have identified two important sources of error in the method: (i) the temporally correlated data, i.e. a minimum sampling time to ensure an adequate convergence to the solution is required and (ii) an underdetermined estimation problem, with more layers' unknowns than independent input points from C_{meas}.

Fig. 15 shows the simulated auto-correlation functions for the European extremely large telescope (E-ELT) and its first light instrument HARMONI (Thatte et al. 2014) consisting of a 39 m aperture that contains 78×78 subaperture grid. An analysis of
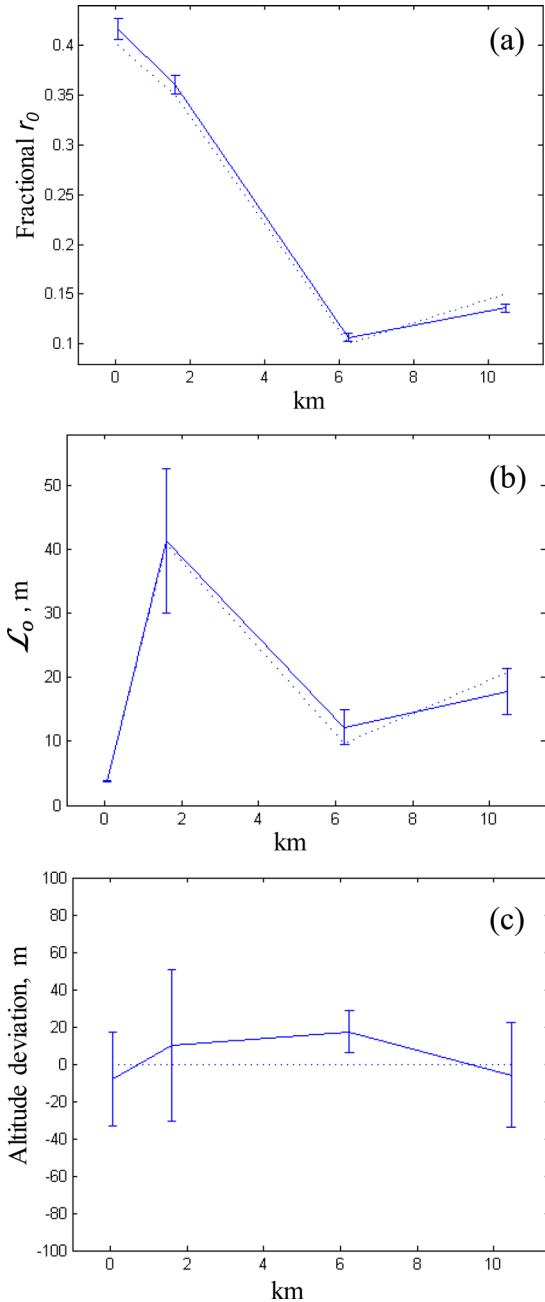
Figure 13. Four-layer turbulence simulated with OOMAO. The panels show the real profiles (dots) and the estimated values (continuous) for the mean values and their respective error bars (standard deviation): (a) fractional r_0; (b) outer scale, $\mathcal{L}_0(h)$; and (c) layer altitude, h.

Figure 14. Mean (continuous line) and median (dotted) for $\mathcal{L}_0(h)$ at Cerro Pachón for 3 yr of campaigns. In many altitude segments, multimode histograms are observed. The magnified bar plot for the first slab (bottom panel) shows two modes at the extremes of the histogram range (1 and 50 m).

this technique for the next generation of these giant telescopes is beyond the scope of this paper. However, a comparison of their auto-correlation functions to those of an 8 m telescope shows that thanks to the five-fold increase in the aperture diameter, the asymptotic convergence of these responses for large $\mathcal{L}_0$ does not exist in this case, allowing better estimates of the turbulence parameters (fractional r_0, $\mathcal{L}_0(h)$ and h), reducing the negative impact of the two error sources studied in Section 3.

In Section 4, we have proposed a procedure to define a minimum length of data and their corresponding sampling rate to guarantee an acceptable error in the estimation of the turbulence parameters,
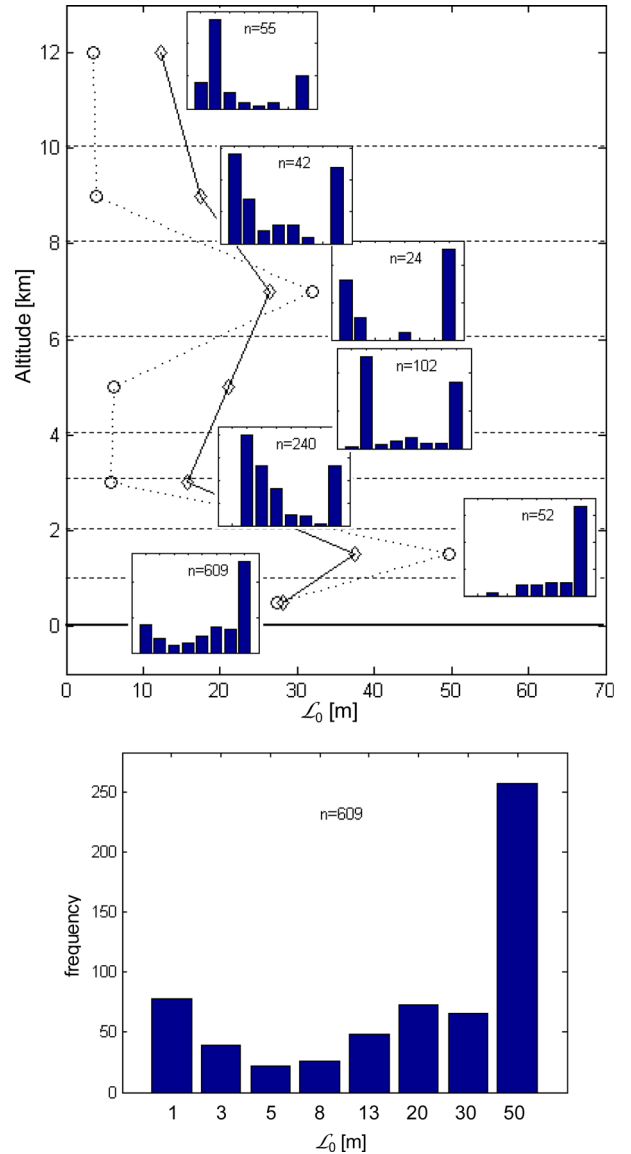
provided that stationarity of turbulence statistics exists throughout the entire observation cycle.

The results presented in this article open up another problem to be tackled in the future, which is the need of appropriate formulae to determine turbulence parameters such as those given in equations (2) and (3) when the outer scale is described by a stratified vector.

Finally, we have developed an analysis (not presented here) of the impact of a stratified outer scale on angular anisoplanatism, where preliminary results show that the degree of decorrelation for angular separation from guiding stars computed from an outer scale profile cannot be fitted by a single scalar-valued $\mathcal{L}_0$. Once more, this stresses the need of knowing $\mathcal{L}_0(h)$ with direct design implications, for instance, in laser-assisted systems whose sky-coverage is a function of tolerable jitter errors hinging on the capability of measuring off-axis tilt within a certain accuracy. The latter involves spatio-angular correlations, themselves a function of the $\mathcal{L}_0(h)$ profile.
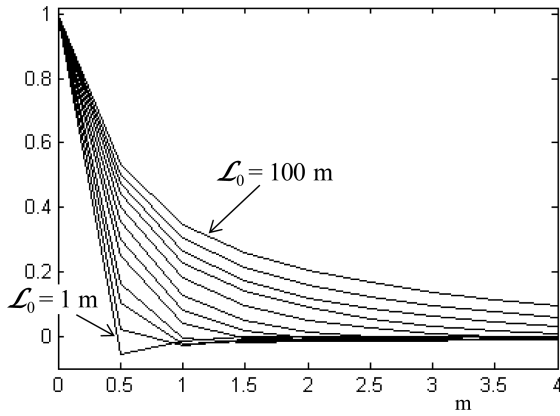
Figure 15. Auto-correlation functions for the E-ELT/HARMONI (Thatte et al. 2014). For large values of $\mathcal{L}_0$ (over 30 m) very distinctive patterns are still observed (see Fig. 1 for comparison). This suggests a substantial reduction in the estimation errors (Section 4) that could be attained in instruments of the next generation of 25–39 m telescopes.

ACKNOWLEDGEMENTS

REFERENCES

Arsenault R. et al., 2012, in Ellerbroek B., Marchetti E., Véran J.-P., eds, Proc. SPIE Conf. Ser. Vol. 8447, Adaptive Optics Systems. SPIE, Bellingham, p. 84470J
Borgnino J., 1990, Appl. Opt., 29, 1863
Borgnino J., Martin F., Ziad A., 1992, Opt. Commun., 91, 267
Butterley T., Wilson R. W., Sarazin M., 2006, MNRAS, 369, 835
Butterley T., Osborn J., Wilson R., 2015, J. Phys. Conf. Ser., 595, 12006
Coleman T. F., Li Y., 1996, SIAM J. Opt., 6, 1040
Conan R., 2000, PhD thesis, Université Nice Sophia Antipolis
Conan R., Correia C., 2014, in Marchetti E., Close L., Véran J.-P., eds, Proc. SPIE Conf. Ser. Vol. 9148, Adaptive Optics Systems IV. SPIE, Bellingham, p. 91486C
Cortés A., Neichel B., Guesalaga A., Osborn J., Rigaut F., Guzmán D., 2012, MNRAS, 427, 2089
Coulman C. E., Vernin J., Coqueugniot Y., Caccia J. L., 1988, Appl. Opt., 27, 155
Dali A. et al., 2010, A&A, 524, A73
Ellerbroek B., 2013, A&A, 552, A41
Fusco T., 2000, PhD thesis, Université de NicemSophia Antipolis
Goodwin M., Jenkins C., Lambert A., 2007, Opt. Express, 15, 14844
Guesalaga A., Neichel B., Cortés A., Béchet C., Guzmán D., 2014, MNRAS, 440, 1925
Jolissaint L., Veran J.-P., Marino J., 2004, Bonaccini D., Ellerbroek B. L., Ragazzoni R., eds, Proc. SPIE Conf. Ser. Vol. 5490, Advancements in Adaptive Optics. SPIE, Bellingham, p. 151
Lardière O. et al., 2014, in Marchetti E., Close L., Véran J.-P., eds, Proc. SPIE Conf. Ser. Vol. 9148, Adaptive Optics Systems IV. SPIE, Bellingham, p. 91481G
Lukin V. P., Fortes B. V., Nosov E. V., 1998, in Bonaccini D., Tyson R. K., eds, Proc. SPIE Conf. Ser. Vol. 3353 Adaptive Optical System Technologies. SPIE, Bellingham, p. 1121
Maire J., Ziad A., Borgnino J., Martin F., 2007, MNRAS, 377, 1236
Martin F. et al., 2000, A&AS, 144, 39
Mazzoni T., Busoni L., Bonaglia M., Esposito S., 2014, in Marchetti E., Close L., Véran J.-P., eds, Proc. SPIE Conf. Ser. Vol. 9148, Adaptive Optics Systems IV. SPIE, Bellingham, p. 91486A
Moré J. J., Sorensen D. C., 1983, SIAM J. Sci. Stat. Comp., 3, 553
Morris T. et al., 2014, in Marchetti E., Close L., Véran J.-P., eds, Proc. SPIE Conf. Ser. Vol. 9148, Adaptive Optics Systems IV. SPIE, Bellingham, p. 91481I
Neichel B. et al., 2010, in Ellerbroek B. L., Hart M., Hubin N., Wizinovich P. L., eds, Proc. SPIE Conf. Ser. Vol. 7736, Adaptive Optics Systems II. SPIE, Bellingham, p. 773606
Ragazzoni R., Marchetti E., Valente G., 2000, Nature, 403, 54
Schmidt D. et al., 2014, in Marchetti E., Close L., Véran J.-P., eds, Proc. SPIE Conf. Ser. Vol. 9148, Adaptive Optics Systems IV. SPIE, Bellingham, p. 91482U
Thatte N. A. et al., 2014, in Ramsay S. K., McLean I. S., Takami H., eds, Proc. SPIE Conf. Ser. Vol. 9147, Ground-based and Airborne Instrumentation for Astronomy V. SPIE, Bellingham, p. 914725
Tokovinin A., 2002, PASP, 114, 1156
Tokovinin A., Kornilov V., 2007, MNRAS, 381, 1179
Wang L., Schöck M., Chanan G., 2008, Appl. Opt., 47, 1880
Yelda S., Meyer L., Ghez A., Do T., 2013, in Esposito S., Luca F., eds., Proc. 3rd AO4ELT Conf. p. 13371. Available at: http://ao4elt3.arcetri.astro.it/proceedings
Ziad A., 2016, in Marchetti E., Close L. M., Véran J.-P., eds, Proc. SPIE Conf. Ser. Vol. 9909, Adaptive Optics Systems IV. SPIE, Bellingham, p. 99091K
Ziad A. et al., 2013, in Esposito S., Luca F., eds., Proc. 3rd AO4ELT Conf.. p. 21355. Available at: http://ao4elt3.arcetri.astro.it/proceedings

APPENDIX: NOISE ESTIMATION

Spatial noise from the WFS detector pixels matches perfectly with auto-correlation maps, generating peaks in the centre of the auto-correlation maps that causes an underestimation of the integrated outer scale, i.e. extremely narrow responses (those corresponding to small $\mathcal{L}_0$ values) become similar to noise auto-correlations. Hence, a reliable method of noise estimation is necessary to mitigate its distorting effects on the fitting. This distortion is particularly important in methods that fit theoretical auto-correlation functions to those from on-sky data that generally leave out the central correlation component (see Fig. A1). Unfortunately, we have found that unacceptable errors can occur when the turbulence is formed by more than one layer with different outer scales.

A noise estimation can also be extracted from the power spectral density of AO residual slopes at the higher end of the spectrum, where noise dominates. The weakness here is that vibration peaks and turbulence components from fast winds can contaminate this segment of the spectrum, generating significant errors in the estimation.

We have found that the best method to estimate the noise is the one shown in Fig. A2, which uses the correlation of slopes but with a one-frame delay, assuming that no temporal correlation of noise exists between successive frames. In our experience, this is by far
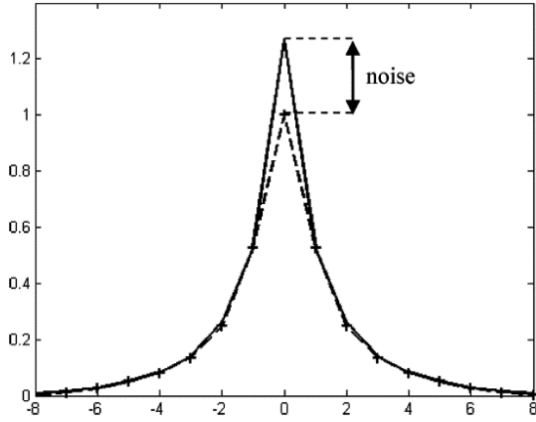
Figure A1. Fitting theoretical auto-correlation functions to measured auto-correlation maps (continuous line: on-sky data; dotted line: theoretical function). By leaving the central component out of the fitting process, the noise can be determined from the difference between the two functions at the centre element.

the most reliable and accurate method, as long as either a high frame rate is used or the wind speed is low for all layers. In other words, the product of the frame rate times the wind speed must be substantially smaller than the size of the subaperture diameter. For
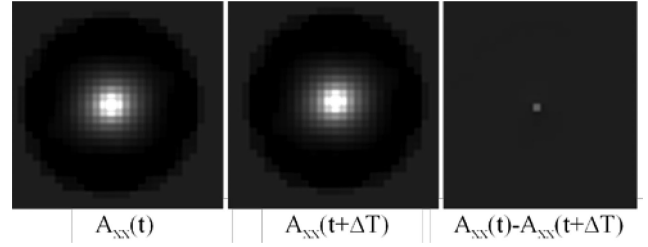

Figure A2. Auto-correlations between slopes from the same WFS: simultaneous frames (left); correlation between two consecutive frames (centre); and respective difference error (right), from which the noise can be estimated.

example, with GeMS operating at 500 Hz and a maximum wind speed of 20 m s^{-1}, this product is 0.04 m, much smaller than a subaperture diameter of 0.5 m.

This paper has been typeset from a Microsoft Word file prepared by the author.